Muscle-like fatigue-resistant hydrogels by mechanical training

Shaoting Lin[a,1], Ji Liu[a,1], Xinyue Liu[a], and Xuanhe Zhao[a,b,2]

[a]Department of Mechanical Engineering, Massachusetts Institute of Technology, Cambridge, MA 02139; and [b]Department of Civil and Environmental Engineering, Massachusetts Institute of Technology, Cambridge, MA 02139

Edited by David A. Weitz, Harvard University, Cambridge, MA, and approved April 8, 2019 (received for review February 20, 2019)

Skeletal muscles possess the combinational properties of high fatigue resistance (1,000 J/m^2), high strength (1 MPa), low Young's modulus (100 kPa), and high water content (70 to 80 wt %), which have not been achieved in synthetic hydrogels. The muscle-like properties are highly desirable for hydrogels' nascent applications in load-bearing artificial tissues and soft devices. Here, we propose a strategy of mechanical training to achieve the aligned nanofibrillar architectures of skeletal muscles in synthetic hydrogels, resulting in the combinational muscle-like properties. These properties are obtained through the training-induced alignment of nanofibrils, without additional chemical modifications or additives. In situ confocal microscopy of the hydrogels' fracturing processes reveals that the fatigue resistance results from the crack pinning by the aligned nanofibrils, which require much higher energy to fracture than the corresponding amorphous polymer chains. This strategy is particularly applicable for 3D-printed microstructures of hydrogels, in which we can achieve isotropically fatigue-resistant, strong yet compliant properties.

polyvinyl alcohol | anti–fatigue-fracture | freeze–thaw | prestretch | 3D printing

Biological load-bearing tissues such as skeletal muscles commonly show J-shaped stress–strain behaviors with low Young's modulus and high strength on the order of 100 kPa and 1 MPa, respectively (1, 2). Moreover, despite their high water content of around 75 wt % (3), skeletal muscles can sustain a high stress of 1 MPa over 1 million cycles per year, with a fatigue resistance over 1,000 J/m^2 (4). The combinational properties of skeletal muscles (i.e., high fatigue resistance, high strength, superior compliance, and high water content) are highly desirable for hydrogels' nascent applications in soft biological devices, such as load-bearing artificial tissues (5), hydrogel bioelectronics (6–9), hydrogel optical fibers (10, 11), ingestible hydrogel devices (12), robust hydrogel coatings on medical devices (13–17), and hydrogel soft robots (18–20).

Although various molecular and macromolecular engineering approaches have replicated parts of biological muscles' characteristics, none of them can synergistically replicate all these attributes in one single material system (*SI Appendix*, Table S1). For example, both strain-stiffening hydrogels (21, 22) and bottle brush polymer networks (1, 23) can mimic the J-shaped stress–strain behaviors, but their fracture toughness is still much lower than biological tissues, since no significant mechanical dissipation has been introduced in these materials for toughness enhancement. Although various tough hydrogels (24–26) have been developed by incorporating various dissipation mechanisms, they are susceptible to fatigue fracture under repeated mechanical loads, since the resistance to fatigue crack propagation after prolonged repeated mechanical loads is the energy required to fracture a single layer of polymer chains, unaffected by the additional dissipation (27). Recently, introduction of well-controlled nanocrystalline domains (28) has been shown to substantially increase a hydrogel's fatigue threshold (i.e., the minimal fracture energy at which crack propagation occurs under cyclic loads), but the growth of nanocrystalline domains consumes interstitial amorphous polymer chains and therefore increases the Young's modulus and reduces the water content of the hydrogel.

Here, we propose a strategy to achieve the combinational muscle-like properties in synthetic hydrogels via mechanical training (Fig. 1*A*). Using freeze-thawed polyvinyl alcohol (PVA) hydrogel as a model material, we successfully mimic the aligned nanofibrillar architectures in skeletal muscles (Fig. 1*B*). The developed hydrogels by mechanical training can achieve an extremely high fatigue threshold (1,250 J/m^2) and nominal tensile strength (5.2 MPa), while maintaining a high water content (84 wt %) and low Young's modulus (200 kPa), reaching combinational muscle-level properties (29) (Fig. 1*C*). In situ confocal microscopy of the hydrogels' fracturing processes reveals that the fatigue-resistant (or anti–fatigue-fracture, endurant) mechanism for the hydrogels is the crack pinning by the aligned nanofibrils, which require much higher energy to fracture than the corresponding amorphous polymer chains. In situ X-ray scattering of the hydrogels under elongation further reveals that the low Young's modulus of the hydrogels is attributed to the stretching of polymer chains, orientation of nanocrystalline domains, and sliding of aligned nanofibrils under moderate stretches.

Results

Design of Muscle-Like Hydrogels. Fig. 1*A* schematically illustrates our strategy to design synthetic hydrogels with combinational properties comparable to skeletal muscles. The strategy first involves growing compliant nanofibrils in PVA hydrogels by forming two separated phases (30): (*i*) high concentration of polymer chains in the form of nanofibrils cross-linked by

Significance

The combinational muscle-like properties including high fatigue resistance, high strength, superior compliance, and high water content are highly desirable for various applications of soft biomaterials such as hydrogels. These combinational properties, largely attributed to the aligned nanofibrils in natural muscles, have not been achieved in synthetic hydrogels. Here, we propose a strategy of mechanical training to impart hydrogels with an extremely high fatigue threshold (1,250 J/m^2) and strength (5.2 MPa), while maintaining a high water content (84 wt %) and a low Young's modulus (200 kPa), reaching combinational muscle-like properties with aligned nanofibrillar architectures. We further achieve isotropically enhanced properties by three-dimensionally printing the hydrogels into microstructures.

Author contributions: S.L., J.L., and X.Z. designed research; S.L., J.L., X.L., and X.Z. performed research; S.L., J.L., X.L., and X.Z. analyzed data; and S.L., J.L., X.L., and X.Z. wrote the paper.

The authors declare no conflict of interest.

This article is a PNAS Direct Submission.

[1]S.L. and J.L. contributed equally to this work.

[2]To whom correspondence should be addressed. Email: zhaox@mit.edu.

This article contains supporting information online at www.pnas.org/lookup/suppl/doi:10.1073/pnas.1903019116/-/DCSupplemental.

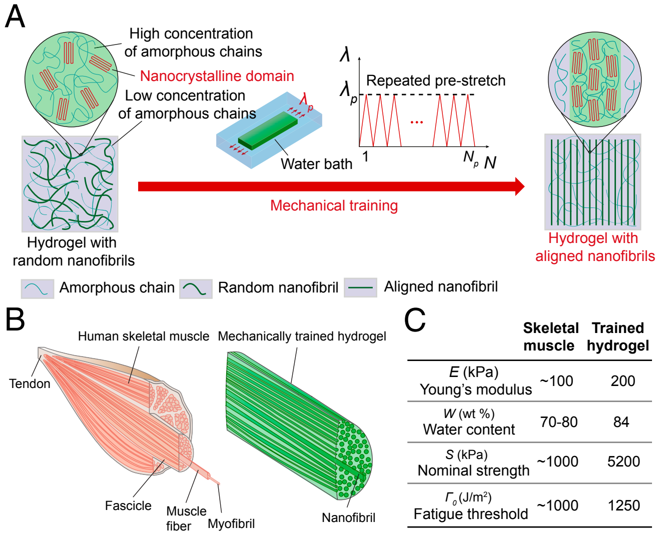

	Skeletal muscle	Trained hydrogel
E (kPa) Young's modulus	~100	200
W (wt %) Water content	70-80	84
S (kPa) Nominal strength	~1000	5200
Γ_0 (J/m²) Fatigue threshold	~1000	1250

Fig. 1. Design of muscle-like hydrogels. (*A*) Schematic illustration of the microstructure of a PVA hydrogel with randomly oriented nanofibrils before mechanical training and a PVA hydrogel with aligned nanofibrils after mechanical training (i.e., cyclic prestretches). (*B*) Similar aligned nanofibrillar architectures of human skeletal muscles and mechanically trained hydrogels. (*C*) Comparison of combinational properties of human skeletal muscle and mechanically trained hydrogel.

nanocrystalline domains and (*ii*) low concentration of amorphous polymer chains. PVA polymer chains possess abundant hydroxyl side groups, which can readily form intrachain/interchain hydrogen bonding. Upon exposure to a low temperature below freezing (i.e., −20 °C), the water freezes and forms ice crystals that can expel PVA chains to form regions of high polymer concentrations. As the PVA chains come into close contact with each other, nanocrystalline domains nucleate with the formation of hydrogen bonds (30–32). These interactions (i.e., hydrogen bonding) remain intact in the subsequent thawing process, leading to a physically cross-linked network of nanofibrils. The dendritic growth of ice crystals further leads to a random distribution of these nanofibrils (33). The process of freezing and thawing is repeated for five cycles to grow sufficient nanofibrils.

To form the aligned nanofibrillar structures, the pristine freeze-thawed hydrogels with randomly distributed nanofibrils are exposed to repeated prestretches in a water bath as mechanical training, similar to the exercise of skeletal muscles. Under repeated exercise, skeletal muscles get strengthened by self-growing, accompanied by the disruption of the nanofibrillar structures in skeletal muscle and growth of new muscle nanofibrils (34). Similarly, repeated prestretches applied on the hydrogels with randomly distributed nanofibrils are accompanied by the disruption of randomly oriented nanocrystalline domains, followed by gradual alignment of nanofibrils with newly formed aligned nanocrystalline domains (35). One merit of our training strategy is that it does not require any extra supply of building blocks (i.e., monomers) during the mechanical training (36).

Random and Aligned Nanofibrillar Structures. We first use confocal laser scanning microscopy to visualize the nanofibrils in the pristine freeze-thawed PVA hydrogel. Fluorochromes are conjugated to the PVA macromolecules by immersing the freeze-thawed hydrogels in a reactive dye solution (37) (*SI Appendix*, Fig. S1). With the conjugated fluorochromes, the PVA-rich phases are visible in green in the form of randomly distributed nanofibrils (Fig. 2*A*), while regions with relatively low concentrations of PVA polymers (i.e., water-rich phase between adjacent nanofibrils) are dark. As a control, the chemically cross-linked PVA hydrogel shows green luminance with uniform brightness, indicating the uniform distribution of PVA amorphous chains (*SI Appendix*, Fig. S2).

We next show that the freeze-thawed PVA hydrogel can form aligned nanofibrillar structures by repeated prestretches in a water bath (Fig. 2*A* and *SI Appendix*, Fig. S3*A*). The confocal images of the prestretched PVA hydrogel in Fig. 2*A* and *SI Appendix*, Fig. S3 confirm that the randomly distributed nanofibrils gradually reorient and align toward the direction of the applied prestretches. It is noted that, once the first cycle of prestretch is relaxed, the aligned nanofibrils mostly recover their previous random distribution elastically (*SI Appendix*, Fig. S4). As the cycle number increases, plastic deformation accumulates in the hydrogel, which gradually elongates along the prestretched direction, and finally preserves the alignment (*SI Appendix*, Fig. S5). The alignment of nanofibrils reaches a steady state after sufficient cycles of prestretches (i.e., 1,000 cycles of prestretches of 4.6). The alignment of the nanofibrils in the prestretched PVA hydrogels is also validated through scanning electron microscopy (SEM) images (Fig. 2*C*) and atomic force microscopy (AFM) phase images (Fig. 2*D*). Small angle X-ray scanning (SAXS) patterns (Fig. 2*B*) further reveal that the nanocrystalline domains in nanofibrils have been reoriented during the prestretches. In addition, the measured diameters of the nanofibrils range from ∼100 nm to ∼1 μm (Fig. 2 *A* and *C* and *SI Appendix*, Fig. S6).

Existing approaches to introduce ordered nanocrystalline domains and aligned structures in hydrogels include cold-drawing (38), prestretching in air (39), and constrained air-drying (40), which fail to retain their original high water contents, due to the formation of additional excessive nanocrystalline domains. By contrast, the prestretched PVA hydrogel obtained from our strategy can still maintain a high water content of 84 wt % (Fig. 3*C*), close to the pristine freeze-thawed PVA samples (88 wt %). The differential scanning calorimetry results further show that the crystallinity in the swollen state of the prestretched PVA hydrogel is only 2.8 wt % (*SI Appendix*, Fig. S8), slightly higher than the pristine freeze-thawed PVA hydrogel (1.8 wt %) (Fig. 3*C*). The slightly increased crystallinity could be attributed to the newly formed nanocrystalline domains during the nanofibrillar alignments under cyclic prestretches (41). Both high water content and low crystallinity in our prestretched PVA hydrogel indicate that our strategy could substantially suppress the undesirable excessive

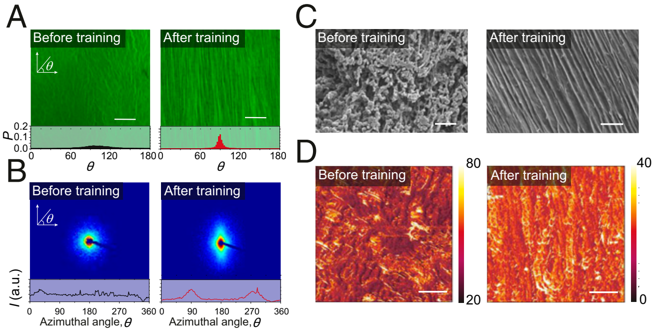

Fig. 2. Microstructures of PVA hydrogels before and after mechanical training. (*A*) Confocal images and corresponding histograms of a hydrogel with randomly oriented nanofibrils before training (i.e., freeze-thawed PVA) and a hydrogel with aligned nanofibrils after training (i.e., prestretched PVA). *P* in the histograms represents the probability of nanofibrils at each aligned direction θ. (Scale bar: 50 μm.) (*B*) SAXS patterns and corresponding scattering intensity I vs. azimuthal angle θ curve of a hydrogel with randomly oriented nanofibrils before training (i.e., freeze-thawed PVA) and hydrogel with aligned nanofibrils after training (i.e., prestretched PVA); a.u., arbitrary units. (*C*) SEM images of a hydrogel with randomly oriented nanofibrils before training (i.e., freeze-thawed PVA) and a hydrogel with aligned nanofibrils after training (i.e., prestretched PVA). [Scale bars: 20 μm (*Left*), 10 μm (*Right*).] (*D*) AFM phase images of a hydrogel with randomly oriented nanofibrils before training (i.e., freeze-thawed PVA) and a hydrogel with aligned nanofibrils after training (i.e., prestretched PVA). (Scale bar: 100 nm.)

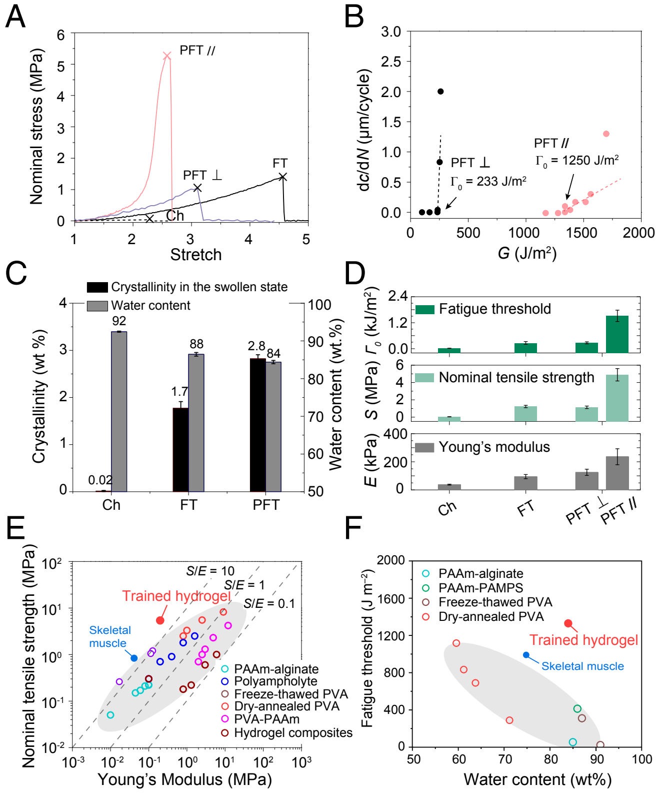

Fig. 3. Mechanical properties of PVA hydrogels before and after mechanical training. (*A*) Nominal stress versus stretch curves of chemically cross-linked (Ch), freeze-thawed (FT), and prestretched PVA hydrogels parallel to (PFT //) and perpendicular to (PFT ⊥) nanofibrils. The X mark indicates the point of fracture. (*B*) Crack extension per cycle dc/dN versus applied energy release rate G of prestretched PVA hydrogels parallel to (PFT //) and perpendicular to (PFT ⊥) nanofibrils. (*C*) Summarized water contents and crystallinities in the swollen state of chemically cross-linked PVA (Ch), freeze-thawed PVA (FT), and prestretched PVA (PFT). (*D*) Summarized Young's moduli E, ultimate nominal tensile strengths S, and fatigue thresholds Γ_0 of chemically cross-linked (Ch), freeze-thawed (FT) and prestretched PVA hydrogels parallel to (PFT //) and perpendicular to (PFT ⊥) nanofibrils. (*E*) Comparison chart in the plot of nominal tensile strengths and Young's moduli among tough hydrogels [e.g., PAAm-alginate (24), polyampholyte (47), freeze-thawed PVA (28), dry-annealed PVA (28), PVA-PAAm (48), and hydrogel composites (51)], biological tissues [e.g., skeletal muscle (1, 2)], and trained hydrogel (i.e., prestretched PVA). The dashed lines denote the linear relation between strength and modulus with strength–modulus ratio S/E of 0.1, 1, and 10. (*F*) Comparison chart in the plot of fatigue thresholds and water contents among tough hydrogels (44) [e.g., PAAm-alginate, PAAm-poly(2-acrylamido-2-methylpropanesulfonic acid) (PAMPS), freeze-thawed PVA] and nanocrystalline hydrogels (e.g., dry-annealed PVA) (28), biological tissues (e.g., skeletal muscle), and trained hydrogel (i.e., prestretched PVA). Data in *C* and *D* are means ± SD, $n = 3$.

crystallization while maintaining water content and compliance of the hydrogels.

Combinational Muscle-Like Properties. We further demonstrate the combinational muscle-like mechanical properties in the prestretched PVA hydrogel (Fig. 3). At small stretches, the prestretched PVA hydrogel demonstrates a low Young's modulus along directions both parallel (210 kPa) and perpendicular (140 kPa) to the aligned nanofibrils, similar to the pristine freeze-thawed PVA hydrogel (100 kPa) (Fig. 3 *A* and *D*). At high stretches, the prestretched PVA hydrogel stiffens drastically parallel to the aligned nanofibrils, exhibiting a J-shaped stress versus stretch curve, similar to that of skeletal muscles (1). In addition, the prestretched PVA hydrogel shows an extremely high ultimate nominal tensile strength of 5.2 MPa parallel to the aligned nanofibrils, which is 4.3 times the pristine freeze-thawed hydrogel's strength (1.2 MPa) and 26 times the chemically cross-linked hydrogel's strength (0.2 MPa) (Fig. 3 *A* and *D*). The ultimate nominal tensile strength of the prestretched PVA hydrogel perpendicular to nanofibrils is measured to be 1.1 MPa, close to the value of the pristine freeze-thawed hydrogel (i.e., 1.2 MPa). The prestretched PVA hydrogel also shows high resilience with negligible hysteresis when stretched along the aligned nanofibrils (*SI Appendix*, Fig. S9). The fatigue threshold of the prestretched PVA hydrogel measured along the aligned nanofibrils reaches a record-high value of 1,250 J/m^2 (Fig. 3*B*), orders of magnitude higher than those of existing tough hydrogels (∼10 J/m^2 to ∼100 J/m^2) (42–44). To validate the high fatigue threshold of the prestretched PVA hydrogels parallel to the aligned nanofibrils, we also apply cyclic loads on a single-notch tensile specimen with an energy release rate of 1,250 J/m^2 and observe no crack extension over 30,000 cycles (*SI Appendix*, Fig. S10). Note that the resolution of measured dc/dN to determine this fatigue threshold is on the same order as the resolution in previous measurements of rubbers' fatigue thresholds (27). By contrast, the fatigue threshold perpendicular to the aligned nanofibrils is 233 J/m^2, which is on the same order as that of the pristine freeze-thawed PVA hydrogel (i.e., 310 J/m^2; *SI Appendix*, Fig. S11), but still much larger than that of the chemically cross-linked PVA hydrogel (i.e., 10 J/m^2; *SI Appendix*, Fig. S11).

To compare our results with existing hydrogels and biological tissues, we summarize the nominal tensile strengths, Young's moduli, fatigue thresholds, and water contents of various tough hydrogels (24, 25, 28, 40, 45–49) and biological tissues (1) in Fig. 3 *E* and *F*. The strength−modulus ratios S/E of existing tough hydrogels such as PAAm-alginate (24), PVA-PAAm (48), dry annealed PVA (28), freeze-thawed PVA (50), polyampholyte hydrogels (47), fiber-reinforced hydrogel composites (45, 51), wood hydrogels (46), and constrained air-drying hydrogels (40) are in the range of 0.1 to 10 (Fig. 3*E*). Remarkably, the strength−modulus ratio S/E of the prestretched PVA hydrogel is as high as 50, since the high strength of the prestretched PVA hydrogel is accompanied by its low Young's modulus.

In addition to the challenge of designing synthetic hydrogels with superior compliance and high strength, the combinational properties of high fatigue threshold and high water content have not been achieved in existing hydrogels (Fig. 3*F*). By following our strategy, the fatigue threshold of the prestretched PVA hydrogel can achieve a high value of 1,250 J/m^2 along with a high water content of 84 wt %, outperforming existing hydrogels and biological tissues.

Mechanisms for Superior Compliance. In situ SAXS measurements offer insights into the mechanisms for the superior compliance of the prestretched PVA hydrogel at small deformations (Fig. 4*A*). The nanocrystalline morphology in the prestretched PVA hydrogel (in the swollen state) is investigated by SAXS analysis at the applied stretch of 1, 1.4, 1.8, and 2.2. As shown in Fig. 4 *B* and *D*, the average distance between neighboring nanocrystalline domains parallel to aligned nanofibrils $L_{//}$ (i.e., $\theta = 0°$) for the prestretched PVA hydrogel at undeformed state (i.e., $\lambda = 1$) is estimated to be 13.2 nm. As the applied stretch increases to 2.2, the average distance between neighboring nanocrystalline domains increases to 15.5 nm (Fig. 4*D*), which indicates the stretching of interstitial amorphous chains between the adjacent nanocrystalline domains in the nanofibrils. Since the stretch ratio of interstitial amorphous chains (e.g., 15.5 nm/13.2 nm) is much lower than the corresponding applied stretch (e.g., 2.2), sliding between nanofibrils may also occur during stretching. In comparison, the scattering curves show negligible difference at different stretches perpendicular to the aligned nanofibrils $L\perp$ (i.e., $\theta = 90°$) (Fig. 4*C*), which implies the average distance between neighboring nanocrystalline domains perpendicular to the aligned nanofibrils $L\perp$ (i.e., $\theta = 90°$) remains constant with negligible lateral contraction as the stretch increases.

We further plot the scattering intensity I versus direction θ to quantify the degree of orientation of nanocrystalline domains during stretching (Fig. 4*E*). At the undeformed state (i.e., $\lambda = 1$),

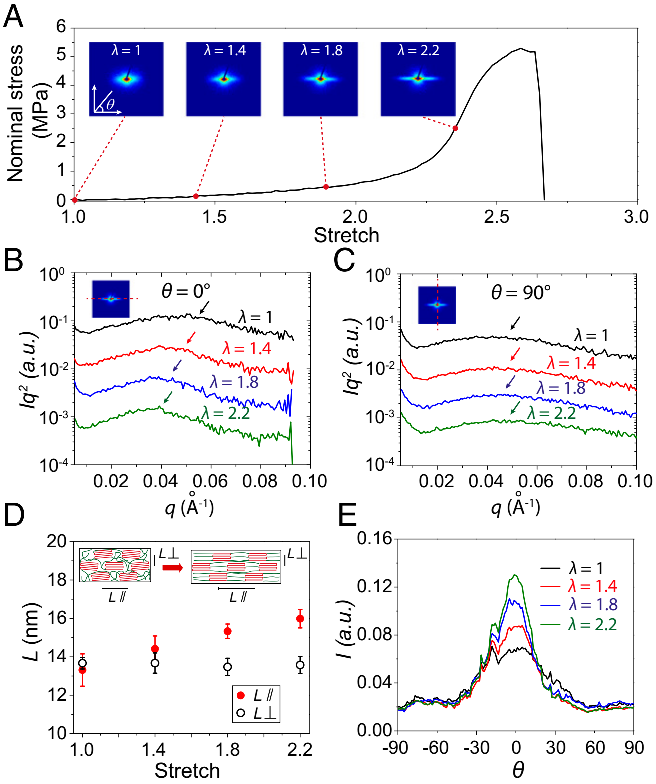

Fig. 4. Mechanisms for high compliance of prestretched PVA hydrogel with aligned nanofibrils. (*A*) Nominal stress versus stretch curve of prestretched PVA hydrogel with aligned nanofibrils and corresponding SAXS pattern at the stretch of 1, 1.4, 1.8, and 2.2. (*B*) The corrected scattering intensity Iq^2 versus vector q parallel to nanofibrils (i.e., $\theta = 0°$) of prestretched PVA hydrogel at the stretch of 1, 1.4, 1.8, and 2.2. (*C*) The corrected scattering intensity Iq^2 versus vector q perpendicular to nanofibrils (i.e., $\theta = 90°$) of prestretched PVA hydrogel at the stretch of 1, 1.4, 1.8, and 2.2. (*D*) Calculated average distance between adjacent nanocrystalline domains of prestretched PVA hydrogel parallel to nanofibrils *L//* (i.e., $\theta = 0°$) and perpendicular to nanofibrils $L\perp$ (i.e., $\theta = 90°$) at the stretch of 1, 1.4, 1.8, and 2.2. The *Inset* schematic of nanofibrils illustrates the average distance between adjacent nanocrystalline domains parallel to nanofibrils L//and perpendicuar to nanofibrils L⊥. (*E*) The measured scattering intensity I vs. Azimuthal angle θ curves of prestretched PVA hydrogel at the stretch of 1, 1.4, 1.8, and 2.2. Data in *D* are means ± SD, $n = 3$. The dashed red lines in *Inset* scattering pattern in *B* and *C* indicate the direction parallel to nanofibrils and perpendicular to nanofibrils, respectively.

there are peaks along the prestretched direction (i.e., $\theta = 0°$), implying that the orientation of nanocrystalline domains along the prestretched direction exists in the undeformed sample. As the applied stretch increases, the peaks along the prestretched direction (i.e., $\theta = 0°$) become more pronounced, indicating that the applied stretch can drive additional orientation of nanocrystalline domains. Overall, the stretching of interstitial amorphous chains, orientation of nanocrystalline domains, and sliding between nanofibrils account for the superior compliance of the prestretched PVA hydrogel at moderate deformations along the aligned nanofibrils.

Furthermore, the high compliance of the pristine freeze-thawed PVA hydrogel and the prestretched PVA hydrogel stretched perpendicularly to the aligned nanofibrils can be attributed to the orientation of randomly distributed nanofibrils and the stretching of amorphous polymer chains between adjacent nanofibrils, respectively.

Mechanisms for High Fatigue Threshold. In situ confocal laser scanning microscopy further explains the mechanisms for the high fatigue threshold of the prestretched PVA hydrogel. As shown in Fig. 5 *A* and *B*, the aligned nanofibrils are perpendicular to the crack path and pin the crack due to the high strength of the nanofibrils. There is no observable crack propagation at the applied stretch of 2.4. As the applied stretch further increases to 2.6, the nanofibrils at the crack tip are pulled out from the hydrogel but still bridge the crack tip. As the crack propagates, the rupture of the nanofibrils requires a much higher energy per unit area than fracturing the corresponding amorphous polymer chains, giving rise to a much higher fatigue threshold (1,250 J/m^2) than that of the amorphous polymer networks (10 J/m^2). Notably, the crack pinned by the aligned nanofibrils does not branch or tilt under high static and cyclic loads (e.g., Fig. 5*B* and *SI Appendix*, Fig. S10), assuring the hydrogel's high fatigue threshold. By contrast, crack branching and tilting has been observed in hydrogels reinforced by microscale phase separation (52) and in elastomers reinforced by macroscale fibers (53). It will be interesting to study the effects of the reinforcements across different length scales in future.

When the crack is parallel to the aligned nanofibrils, the crack begins to propagate in between neighboring nanofibrils at the applied stretch of 1.5, fracturing interstitial amorphous chains between the adjacent nanofibrils (Fig. 5 *C* and *D*). Similarly, in pristine freeze-thawed PVA hydrogel, the initially randomly oriented nanofibrils gradually align parallel to the crack contour with the increase of the applied stretch, followed by fracturing interstitial amorphous chains (Fig. 5 *E* and *F*). In addition, due to the very long amorphous chains between the adjacent nanofibrils (27), the fatigue thresholds of the pristine freeze-thawed PVA hydrogel and the prestretched PVA hydrogel with a crack along the aligned nanofibrils are still moderately high (310 J/m^2 and 233 J/m^2, respectively; *SI Appendix*, Fig. S11).

Three-Dimensional Printing of Isotropically Fatigue-Resistant, Strong yet Compliant Micromeshes. The aligned nanofibrils give notably anisotropic mechanical behaviors of the prestretched PVA hydrogel, similar to that of skeletal muscles. However, for many applications, it is desirable to achieve isotropically muscle-level properties. Here, we propose to three-dimensionally print microstructures of hydrogels and mechanically train the structures to achieve fatigue-resistant, strong yet compliant properties in both in-plane directions. To demonstrate such potential, we develop PVA ink and print microstructures with square meshes as shown in *SI Appendix*, Fig. S12*A*. The confocal image of the 3D-printed PVA filaments with a diameter of 750 µm shows random distributions of nanofibrils before mechanical training (Fig. 6*A* and *SI Appendix*, Fig. S12*B*). During mechanical training, the printed microstructure undergoes biaxial cyclic prestretches in a water bath (i.e., prestretch of 3.5 over 1,000 cycles). The trained PVA filaments with a reduced diameter of 500 µm (*SI Appendix*, Fig. S12*B*) show pronounced alignments of nanofibrils along the filaments from the confocal images and the SAXS patterns (Fig. 6*B*). We further measure the effective nominal stress (i.e., the force divided by the cross-sectional area of the microstructure) versus stretch of the PVA mesh before and after training. The effective Young's moduli of the prestretched mesh along both in-plane directions are measured to be 70 kPa, which is slightly higher than that of the pristine mesh (Fig. 6*D*). The effective nominal strength of the prestretched mesh along both in-plane directions is measured to be 500 kPa, which is 1.5 times higher than that of the pristine mesh (Fig. 6*E*). We further apply cyclic loads on both meshes before and after training with a notch (Fig. 6*C*), evaluating their effective fatigue thresholds (i.e., the minimal energy release rate at which crack propagation occurs in the mesh under cyclic loads). The effective fatigue threshold of the prestretched mesh after training reaches 1,000 J/m^2 in both in-plane directions, 2 times higher than that of the pristine mesh (Fig. 6*F*).

Conclusions

The classical Lake–Thomas theory predicts that the fatigue threshold of a polymer network is the energy required to fracture a single layer of amorphous polymer chains, on the order of 1 J/m^2 to 100 J/m^2 (27, 54). We have proposed that the design principle for fatigue-resistant (or anti–fatigue-fracture, endurant) hydrogels is to make the fatigue

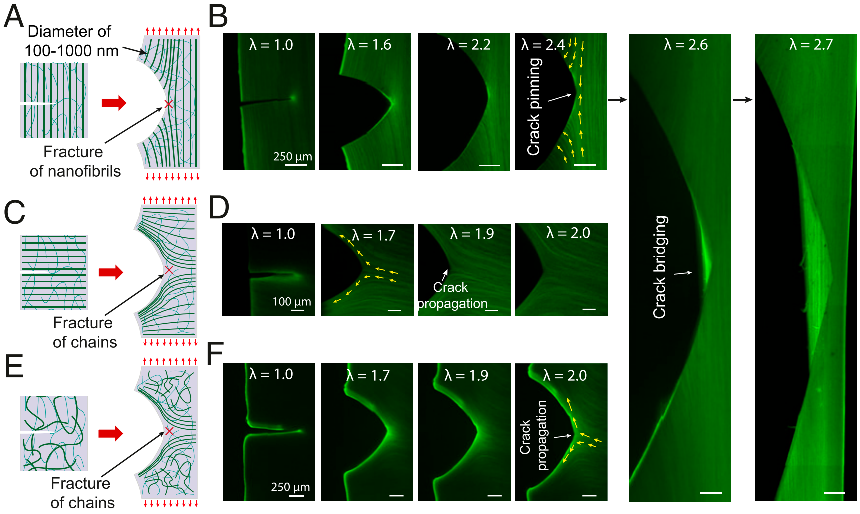

Fig. 5. Mechanisms for high fatigue threshold of prestretched PVA hydrogel with aligned nanofibrils. Schematic illustration of nanofibril morphology in (*A*) notched prestretched PVA hydrogel where crack is perpendicular to the longitudinal direction of nanofibrils, (*C*) notched prestretched PVA hydrogel where crack is parallel to the longitudinal direction of nanofibrils, and (*E*) freeze-thawed PVA hydrogel. Corresponding confocal images of notched samples under different stretches for (*B*) prestretched PVA hydrogel where crack is perpendicular to the longitudinal direction of nanofibrils, (*D*) prestretched PVA hydrogel where crack is parallel to the longitudinal direction of nanofibrils, and (*F*) freeze-thawed PVA hydrogel. The yellow arrows in confocal images indicate the direction of aligned nanofibrils around crack tip. (Scale bars: *B*, 250 μm; *D*, 100 μm; *F*, 250 μm.)

crack encounter and fracture objects requiring energies per unit area much higher than that for fracturing a single layer of amorphous polymer chains (28). We have shown that high densities of nanocrystalline domains in hydrogels can act as the high-energy phase to effectively pin fatigue cracks and greatly enhance the fatigue threshold of nanocrystalline hydrogel up to 1,000 J/m^2, exceeding the Lake–Thomas limit (28). However, the nanocrystalline domains also significantly increase the Young's modulus of the hydrogel, due to nanocrystalline domains' high rigidity over 1 GPa (28).

While a much higher energy is also required to fracture nanofibrils than the corresponding amorphous polymer chains, the rigidity of nanofibrils under moderate stretches can be designed to be relatively low (55). In this paper, we further establish that aligning these nanofibrils in hydrogels by mechanical training can empower the integration of muscle-like performances, i.e., high fatigue threshold (1,250 J/m^2), high strength (5.2 MPa), low Young's modulus (200 kPa), and high water content (84 wt %), into one single hydrogel material. In addition, we achieve isotropically enhanced properties by three-dimensionally printing the hydrogel into microstructures followed by mechanical training. The capability of making strong, fatigue-resistant yet soft hydrogels can enable various biomedical applications that interact with the human body for long-lasting performances. This work also opens an avenue to mechanically engineer alignments of nanofibrils and orientations of nanocrystalline domains in hydrogels.

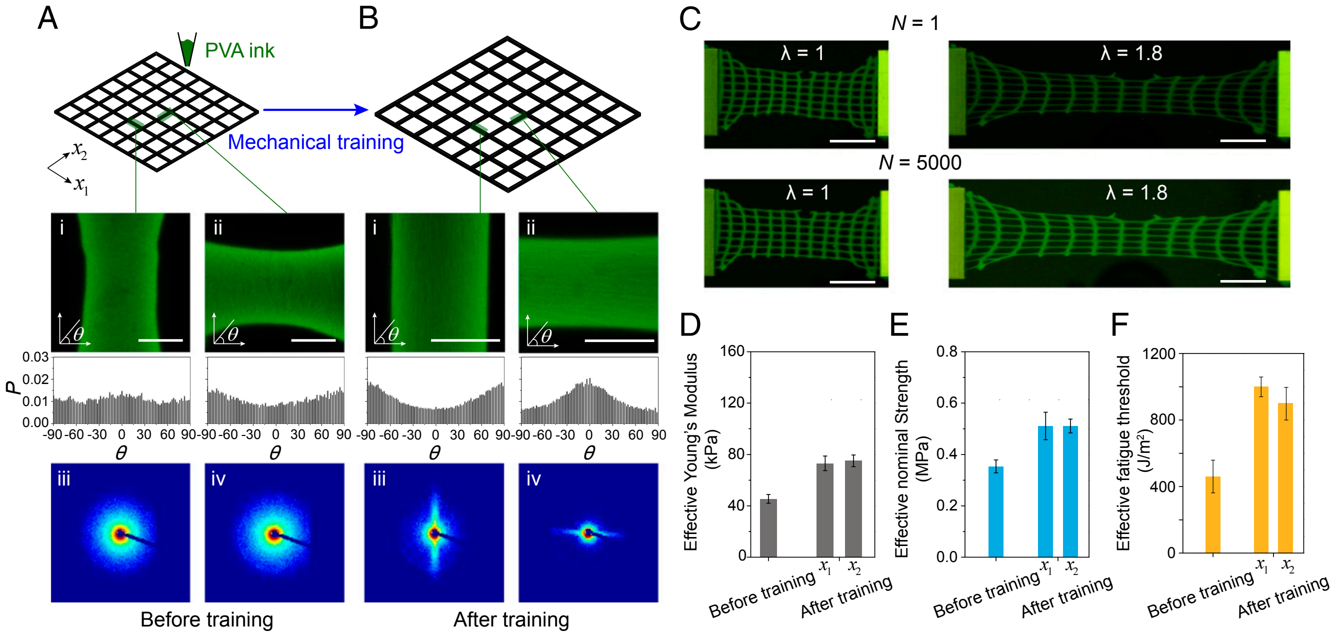

Fig. 6. Isotropically fatigue-resistant, strong yet compliant microstructures of PVA hydrogels by 3D printing and mechanical training. (*A*) Morphology characterization of 3D-printed freeze-thawed PVA mesh before mechanical training: *i* and *ii* are confocal images and histograms for filaments along both in-plane directions; *iii* and *iv* are SAXS patterns in filaments along both in-plane directions. (Scale bar, 250 μm.) (*B*) Morphology characterization of 3D-printed freeze-thawed PVA mesh after mechanical training: *i* and *ii* are confocal images and histograms for filaments along both in-plane directions; *iii* and *iv* are SAXS patterns in filaments along both in-plane directions. (Scale bar, 250 μm.) (*C*) Images of mechanically trained mesh with a precrack at the stretch of 1.0 and 1.8 under the first cycle and the 5,000th cycle of loads. (Scale bar: 1 cm.) (*D*) Effective Young's moduli, (*E*) effective nominal tensile strengths, and (*F*) effective fatigue thresholds of PVA mesh before and after mechanical training. *P* in the histograms in *A* and *B* represents the probability of nanofibrils at each aligned direction θ.

Methods

All details associated with sample preparations, in situ confocal imaging, in situ X-ray scattering, SEM imaging, AFM phase imaging, mechanical characterization, measurement of water content and crystallinity, and 3D printing of PVA meshes appear in *SI Appendix*.

Material Preparation. The freeze-thawed PVA was fabricated by freezing 10 wt % of PVA solution at −20 °C for 8 h and thawing at 25 °C for 3 h with five repeated cycles. The mechanically trained PVA hydrogel was fabricated by cyclically prestretching the freeze-thawed hydrogel in a water bath using a mechanical stretcher (Cellscale).

Confocal Imaging of PVA Hydrogels. To visualize the microstructures of the PVA hydrogels, a fluorescent dye {i.e., 5-[(4,6-dichlorotriazin-2-yl)amino] fluorescein hydrochloride [5-DTAF]} was used to label the PVA side groups. Specifically, PVA hydrogel samples were first immersed in a large volume of sodium bicarbonate solution (0.1 M, pH 9.0) for 12 h to equilibrate the pH within the samples. Then 5 mg of 5-DTAF dissolved in 1.0 mL of anhydrous dimethyl sulfoxide was further immersed into 100 mL of sodium bicarbonate solution (0.1 M, pH 9.0) to form a reactive dye solution. The pH-equilibrated PVA samples were immersed in the dye solution for 12 h at 4 °C in a dark environment to form conjugated fluorochromes. Finally, the hydrogel samples were rinsed several times with deionized water to wash away the nonconjugated dyes, before fluorescence imaging.

Mechanical Characterization. All of the mechanical tests were performed using a U-stretch testing device (Cellscale) at a deformation rate of 0.3/s. Young's modulus, strength, and fatigue threshold were measured in a water bath to prevent dehydration, following the method established in ref. 28.

Three-Dimensional Printing of PVA Hydrogels. The prepared PVA inks were stored in 5-mL syringe barrels, which fit nozzles with diameters of 400 μm (Nordson EFD). To achieve stable and optimal printing, we chose 50 kPa of air pressure (Ultimus V; Nordson EFD) as the printing pressure, and 15 wt % PVA (146 kDa, 99% hydrolysis ratio) as the ink. After deposition, the printed samples were treated by five cycles of freezing (−20 °C for 8 h) and thawing (20 °C for 3 h) to achieve the final PVA hydrogel meshes.

ACKNOWLEDGMENTS. We acknowledge J. Zhou at Massachusetts Institute of Technology (MIT) for help in preparing supercritical drying samples using supercritical dryer (Automegasamdri Series C; Tousimis) at Prof. E. N. Wang's laboratory at MIT, and M. Z. Wyttenbach at MIT for the proofreading. This work was supported by National Science Foundation Grant CMMI-1661627, Office of Naval Research Grant N00014-17-1-2920, and US Army Research Office through the Institute for Soldier Nanotechnologies at MIT, Grant W911NF-13-D-0001.

1. Vatankhah-Varnosfaderani M, et al. (2018) Chameleon-like elastomers with molecularly encoded strain-adaptive stiffening and coloration. *Science* 359:1509–1513.
2. Gillies AR, Lieber RL (2011) Structure and function of the skeletal muscle extracellular matrix. *Muscle Nerve* 44:318–331.
3. Tavichakorntrakool R, et al. (2007) K+, Na+, Mg2+, Ca2+, and water contents in human skeletal muscle: Correlations among these monovalent and divalent cations and their alterations in K+ -depleted subjects. *Transl Res* 150:357–366.
4. Taylor D, O'Mara N, Ryan E, Takaza M, Simms C (2012) The fracture toughness of soft tissues. *J Mech Behav Biomed Mater* 6:139–147.
5. Baker MI, Walsh SP, Schwartz Z, Boyan BD (2012) A review of polyvinyl alcohol and its uses in cartilage and orthopedic applications. *J Biomed Mater Res B Appl Biomater* 100:1451–1457.
6. Zhao S, et al. (2018) Programmable hydrogel ionic circuits for biologically matched electronic interfaces. *Adv Mater* 30:e1800598.
7. Liu Y, et al. (2019) Soft and elastic hydrogel-based microelectronics for localized low-voltage neuromodulation. *Nat Biomed Eng* 3:58–68.
8. Lu B, et al. (2019) Pure PEDOT:PSS hydrogels. *Nat Commun* 10:1043.
9. Yuk H, Lu B, Zhao X (2019) Hydrogel bioelectronics. *Chem Soc Rev* 48:1642–1667.
10. Guo J, et al. (2016) Highly stretchable, strain sensing hydrogel optical fibers. *Adv Mater* 28:10244–10249.
11. Choi M, Humar M, Kim S, Yun SH (2015) Step-index optical fiber made of biocompatible hydrogels. *Adv Mater* 27:4081–4086.
12. Liu X, et al. (2019) Ingestible hydrogel device. *Nat Commun* 10:493.
13. Parada GA, Yuk H, Liu X, Hsieh AJ, Zhao X (2017) Impermeable robust hydrogels via hybrid lamination. *Adv Healthc Mater* 6:1700520.
14. Yuk H, Zhang T, Lin S, Parada GA, Zhao X (2016) Tough bonding of hydrogels to diverse non-porous surfaces. *Nat Mater* 15:190–196.
15. Yuk H, Zhang T, Parada GA, Liu X, Zhao X (2016) Skin-inspired hydrogel-elastomer hybrids with robust interfaces and functional microstructures. *Nat Commun* 7:12028.
16. Takahashi R, et al. (2018) Tough particle-based double network hydrogels for functional solid surface coatings. *Adv Mater Interfaces* 5:1801018.
17. Yu Y, et al. (2019) Multifunctional "hydrogel skins" on diverse polymers with arbitrary shapes. *Adv Mater* 31:e1807101.
18. Yuk H, et al. (2017) Hydraulic hydrogel actuators and robots optically and sonically camouflaged in water. *Nat Commun* 8:14230.
19. Kim Y, Yuk H, Zhao R, Chester SA, Zhao X (2018) Printing ferromagnetic domains for untethered fast-transforming soft materials. *Nature* 558:274–279.
20. Chin SY, et al. (2017) Additive manufacturing of hydrogel-based materials for next-generation implantable medical devices. *Sci Robot* 2:eaah6451.
21. Jaspers M, et al. (2014) Ultra-responsive soft matter from strain-stiffening hydrogels. *Nat Commun* 5:5808.
22. Kouwer PH, et al. (2013) Responsive biomimetic networks from polyisocyanopeptide hydrogels. *Nature* 493:651–655.
23. Vatankhah-Varnosfaderani M, et al. (2017) Mimicking biological stress-strain behaviour with synthetic elastomers. *Nature* 549:497–501.
24. Sun J-Y, et al. (2012) Highly stretchable and tough hydrogels. *Nature* 489:133–136.
25. Gong JP, Katsuyama Y, Kurokawa T, Osada Y (2003) Double-network hydrogels with extremely high mechanical strength. *Adv Mater* 15:1155–1158.
26. Zhao X (2014) Multi-scale multi-mechanism design of tough hydrogels: Building dissipation into stretchy networks. *Soft Matter* 10:672–687.
27. Lake GJ, Lindley PB (1965) The mechanical fatigue limit for rubber. *J Appl Polym Sci* 9:1233–1251.
28. Lin S, et al. (2019) Anti-fatigue-fracture hydrogels. *Sci Adv* 5:eaau8528.
29. Kinloch AJ (2013) *Fracture Behaviour of Polymers* (Springer, New York).
30. Hassan CM, Peppas NA (2000) Structure and morphology of freeze/thawed PVA hydrogels. *Macromolecules* 33:2472–2479.
31. Peppas NA (1975) Turbidimetric studies of aqueous poly (vinyl alcohol) solutions. *Macromol Chem Phys* 176:3433–3440.
32. Holloway JL, Lowman AM, Palmese GR (2013) The role of crystallization and phase separation in the formation of physically cross-linked PVA hydrogels. *Soft Matter* 9:826–833.
33. Willcox PJ, et al. (1999) Microstructure of poly (vinyl alcohol) hydrogels produced by freeze/thaw cycling. *J Polym Sci B* 37:3438–3454.
34. Schoenfeld BJ (2010) The mechanisms of muscle hypertrophy and their application to resistance training. *J Strength Cond Res* 24:2857–2872.
35. Toki S, Fujimaki T, Okuyama M (2000) Strain-induced crystallization of natural rubber as detected real-time by wide-angle X-ray diffraction technique. *Polymer (Guildf)* 41:5423–5429.
36. Matsuda T, Kawakami R, Namba R, Nakajima T, Gong JP (2019) Mechanoresponsive self-growing hydrogels inspired by muscle training. *Science* 363:504–508.
37. Fergg F, Keil F, Quader H (2001) Investigations of the microscopic structure of poly (vinyl alcohol) hydrogels by confocal laser scanning microscopy. *Colloid Polym Sci* 279:61–67.
38. Sehaqui H, et al. (2012) Cellulose nanofiber orientation in nanopaper and nanocomposites by cold drawing. *ACS Appl Mater Interfaces* 4:1043–1049.
39. Fukumori T, Nakaoki T (2015) High strength poly (vinyl alcohol) films obtained by drying and then stretching freeze/thaw cycled gel. *J Appl Polym Sci* 132:41318.
40. Mredha MTI, et al. (2018) A facile method to fabricate anisotropic hydrogels with perfectly aligned hierarchical fibrous structures. *Adv Mater* 30:1704937.
41. Zhang Q, et al. (2018) Stretch-induced structural evolution of poly (vinyl alcohol) film in water at different temperatures: An in-situ synchrotron radiation small-and wide-angle X-ray scattering study. *Polymer (Guildf)* 142:233–243.
42. Bai R, et al. (2017) Fatigue fracture of tough hydrogels. *Extreme Mech Lett* 15:91–96.
43. Zhang W, et al. (2017) Fatigue of double-network hydrogels. *Eng Fract Mech* 187:74–93.
44. Bai R, Yang J, Suo Z (2019) Fatigue of hydrogels. *Eur J Mech A Solids* 74:337–370.
45. Haraguchi K, Takehisa T (2002) Nanocomposite hydrogels: A unique organic–inorganic network structure with extraordinary mechanical, optical, and swelling/de-swelling properties. *Adv Mater* 14:1120–1124.
46. Kong W, et al. (2018) Muscle-inspired highly anisotropic, strong, ion-conductive hydrogels. *Adv Mater* 30:e1801934.
47. Sun TL, et al. (2013) Physical hydrogels composed of polyampholytes demonstrate high toughness and viscoelasticity. *Nat Mater* 12:932–937.
48. Li J, Suo Z, Vlassak JJ (2014) Stiff, strong, and tough hydrogels with good chemical stability. *J Mater Chem B Mater Biol Med* 2:6708–6713.
49. Lin S, Zhou Y, Zhao X (2014) Designing extremely resilient and tough hydrogels via delayed dissipation. *Extreme Mech Lett* 1:70–75.
50. Stauffer SR, Peppast NA (1992) Poly (vinyl alcohol) hydrogels prepared by freezing-thawing cyclic processing. *Polymer (Guildf)* 33:3932–3936.
51. Lin S, et al. (2014) Design of stiff, tough and stretchy hydrogel composites via nanoscale hybrid crosslinking and macroscale fiber reinforcement. *Soft Matter* 10:7519–7527.
52. Bai R, Yang J, Morelle XP, Suo Z (2019) Flaw-insensitive hydrogels under static and cyclic loads. *Macromol Rapid Commun* 2019:e1800883.
53. Wang Z, et al. (2019) Stretchable materials of high toughness and low hysteresis. *Proc Natl Acad Sci USA* 116:5967–5972.
54. Lake GJ, Thomas AG (1967) The strength of highly elastic materials. *Proc R Soc Lond A* 300:108–119.
55. Ling S, Kaplan DL, Buehler MJ (2018) Nanofibrils in nature and materials engineering. *Nat Rev Mater* 3:18016.

Supplementary Information for

Muscle-like Fatigue-resistant Hydrogels by Mechanical Training

Shaoting Lin, Ji Liu, Xinyue Liu, Xuanhe Zhao[†]

[†]Email: zhaox@mit.edu

This PDF file includes:

- Supplementary text
- Table S1
- Figs. S1 to S12
- Caption for movie S1
- References for SI reference citations

Other supplementary materials for this manuscript include the following:

- Movie S1

Supplementary Information Text

www.pnas.org/cgi/doi/10.1073/pnas.1903019116

Materials and Methods

Materials. All PVA hydrogels (i.e., chemically cross-linked, freeze-thawed, and prestretched PVA hydrogels) were synthesized from a 10 wt% poly(vinyl alcohol) (PVA; Mw 146,000-186,000, 99+% hydrolyzed; Sigma-Aldrich, 363065) solution. The solution was heated in a water bath at 100 °C with stirring for 5 hours. To synthesize the chemically cross-linked PVA hydrogel, we added 10 μL glutaraldehyde (25 vol%, Sigma-Aldrich, G6257) as a cross-linker to a 1 mL 10 wt% PVA solution, and added 10 μL hydrochloric acid (36.5-38 wt%, J.T. Baker, 9535-02) as an accelerator into the other 1 mL of 10 wt% PVA solution. We then mixed and defoamed each solution by using a centrifugal mixer (AR-100; Thinky). The final mixtures obtained by mixing then defoaming the two solutions were then casted into a mold and allowed to cure for 2 hours. The chemically cross-linked PVA hydrogel was immersed in deionized water for two days to remove unreacted chemicals. To fabricate the freeze-thawed PVA hydrogel, 10 wt% PVA solutions after mixing and defoaming were poured into a mold, frozen at -20 °C for 8 hours then thawed at 25 °C for 3 hours. The freeze-thawing process was repeated five times. To fabricate the prestreched PVA hydrogel, we cyclically prestretched the freeze-thawed hydrogel in a water bath using a mechanical stretcher (Cellscale, Canada). The sufficiently aligned nanofibrils were achieved by applying the maximum applied stretch of 4.6 for 1000 cycles.

Confocal imaging of PVA hydrogels in wet state. To visualize the microstructures of the PVA hydrogels, a fluorescent dye, 5-([4,6-dichlorotriazin-2-yl]amino)fluorescein hydrochloride (5-DTAF), was used to label the PVA side groups (Fig. S1). Specifically, PVA hydrogel samples were first immersed in a large volume of sodium bicarbonate solution (0.1 M, pH 9.0) for 12 hours to equilibrate the pH within the samples. 5 mg of 5-DTAF dissolved in 1.0 mL of anhydrous dimethyl sulfoxide (DMSO) was further added into 100 mL of the sodium bicarbonate solution

(0.1 M, pH 9.0) to form a reactive dye solution. The pH-equilibrated PVA samples were immersed in the dye solution for 12 hours at 4 °C in a dark environment to form conjugated fluorochromes. Finally, the hydrogel samples were rinsed several times with deionized water to wash away the non-conjugated dyes, prior to fluorescence imaging. The hydrogel microstructures were imaged using a confocal microscope (Leica TCS SP8). Laser intensity, filter sensitivity, and grayscale threshold were adjusted in each application to optimize the contrast of the images. *In situ* fluorescent imaging of the PVA hydrogel samples during uniaxial stretching was conducted using a linear stretcher (Micro Vice Holder, STJ-0116).

X-ray scattering. We investigated nanocrystalline morphologies in nanofibrils of freeze-thawed PVA hydrogels before and after the prestretches through small angle X-ray scattering (SAXS). The X-ray scattering measurements were performed with a Pilatus3R 300K detector (Bruker Nanostar SAXS in X-ray diffraction shared experimental facility). The measured scattering intensity I of PVA hydrogels in the swollen state was corrected by subtracting the water background. A customized linear stretcher was designed to hold the samples at the various stretches for *in situ* X-ray scattering measurements.

SEM imaging. The SEM images were acquired with supercritically-dried samples by a scanning electron microscope (JEOL 5910). We followed the reported experimental protocol to probe the nanoscale structures of the prestretched PVA (1). A notched sample was gradually elongated to a stretch of 2 without obvious crack propagation in order to delaminate the fibrils near the notch. The PVA sample was immediately immersed in a 2.5 wt% glutaraldehyde solution for 3 hours to fix the structure, and dehydrated through a series of alcohol solutions in ascending concentration (30, 50, 70, 90, 95, and 100 vol% twice) in order to avoid non-uniform shrinkage. The dehydrated PVA sample was fractured along the notch using forceps immediately after being frozen in liquid nitrogen. The fractured samples were kept in ethanol and dried in a supercritical dryer (Automegasamdri Series C, Tousimis). The dried fracture surfaces were then sputter coated with gold and observed by SEM (JEOL 5910).

AFM phase imaging. AFM phase images were acquired with an atomic force microscope (MFP-3D, Asylum Research) in tapping mode. Dry freestanding PVA films were directly attached onto the sample stage with double-sided carbon tape. The probe lightly tapped on the sample surface with a recorded phase shift angle of the probe motion relative to a driving oscillator. The bright regions with high phase angles correspond to regions with a relatively high modulus, and the dark regions with low phase angles correspond to regions with a relatively low modulus.

Mechanical characterization. All the mechanical tests were performed in a water bath at 25°C with a U-stretch testing device (CellScale, Canada). For mechanically weak samples (e.g., the chemically cross-linked hydrogel), a load cell with a maximum force of 4.4 N was used; for mechanically strong samples (e.g., the freeze-thawed and prestretched PVA hydrogels), a load cell with a maximum force of 44 N was used. The nominal stress S was measured from the recorded force F divided by width W and thickness t in the swollen state. The stretch was calculated by the applied displacement divided by gauge length of the sample at undeformed state. The Young's modulus was calculated from the initial slope of the nominal stress versus stretch curve. The ultimate tensile strength was identified at the maximum nominal stress when the sample ruptures.

To measure the fatigue threshold of PVA hydrogels, we adopted the single-notch method, which is widely used in fatigue tests of rubbers. All fatigue tests in this study were performed on fully swollen hydrogels immersed in a water bath to prevent the dehydration-induced crack propagation. Cyclic tensile tests were conducted on notched and unnotched samples with identical dogbone shapes. The initial crack length in notched sample was smaller than one-fifth of the width of the sample. The curves of nominal stress S versus stretch λ of the unnotched samples were obtained over Nth cycles with the maximum applied stretch of $\lambda_{\max}$. The strain energy density of the unnotched sample under the Nth cycle with the maximum applied stretch of $\lambda_{\max}$ can be calculated as $W\left(\lambda_{\max}, N\right)=\int_1^{\lambda_{\max}} S d\lambda$. Thereafter, the same maximum applied stretch $\lambda_{\max}$ was applied on the notched sample, and we recorded the crack length at the undeformed state c over cycles using a digital microscope (AM4815ZT, Dino-Lite; resolution, 20 mm/pixel). The applied energy release rate G in the notched sample under the Nth cycle with the maximum applied stretch of $\lambda_{\max}$ can be calculated as $G\left(\lambda_{\max}, N\right)=2k\left(\lambda_{\max}\right)\cdot c\left(N\right)\cdot W\left(\lambda_{\max}, N\right)$, where k is a slowly varying function of the applied stretch as $k=3/\sqrt{\lambda_{\max}}$. By varying the applied stretch of $\lambda_{\max}$, we acquired the curve of crack extension per cycle dc/dN versus the applied energy release rate G. The fatigue threshold can be obtained by linearly extrapolating the curve of dc/dN vs. G to the intercept with the abscissa. Considering the resolution of the camera is around 0.02 mm (20 μm/pixel for the camera), the detectable resolution of dc/dN is 0.002 μm/cycle for our setup, which is on the same order as the resolution in previous fatigue tests for fatigue thresholds of rubbers (i.e., 0.001 μm/cycle) (2). Unlike bulk PVA samples, there was no detectable fatigue-crack propagation in 3D-printed micro-meshes with a notch (that is, if the crack does not propagate during the 1st cycle in the 3D-printed micro-meshes, it will not propagate over subsequent cycles unless a higher stretch is applied), possibly because the filaments were trained and became stronger during cyclic fatigue measurements. This observation was consistent with the recent work on the design of stretchable materials with high toughness and high resilience (3).

Measurement of water content. We measured the water content in swollen PVA hydrogels using thermal gravimetric analysis (furnace: TGA1-0075, control unit: DCC1-00177). We first cut a disk shape of swollen PVA hydrogels of 3-7 mg. The swollen hydrogels weighing $m_{swollen}$ in a titanium pan without any water droplet on the surface of the samples. The samples were thereafter heated up from 30 °C to 150 °C at the rate of 20 °C/min, and then 150 °C to 160 °C at the rate of 5 °C/min under a nitrogen atmosphere at a flow rate of 30 mL/min. The measured mass of the sample was recorded. In Fig. S7, a typical TGA curve of pristine freeze-thawed PVA hydrogels is plotted. The mass of the sample decreases with the increase of temperature and gradually reaches a plateau m_{dry} when the all residual water in the sample evaporates. The water contents of the swollen PVA hydrogels ϕ_{water} were identified using $1 - m_{dry} / m_{swollen}$.

Measurement of crystallinities. We measured the crystallinities of the resultant PVA hydrogels using differential scanning calorimetry (DSC/cell: RCS1-3277, cooling system: DSC1-0107), following the experimental protocols in the paper (4). Before air-drying the PVA hydrogels for DSC measurements, we first used excess chemical cross-links to fix the amorphous polymer chains to minimize the further formation of crystalline domains during the air-drying process. Specifically, we soaked the samples (thickness of 1 mm) in the aqueous solution consisting of 10 mL of glutaraldehyde (25 vol%;), 500 μL of hydrochloric acid (36.5 to 38 wt%), and 100 mL of DI water for 1 hour. Thereafter, we soaked the samples in a deionized water bath for 1 hour to remove the extra glutaraldehyde and hydrochloric acid. The samples were further dried in an incubator (New Brunswick Scientific, C25) at 37 °C for 1 hour.

In a typical DSC measurement, we first weighed the total mass of the air-dried sample m (still with residual water). The sample was thereafter placed in a Tzero pan and heated up from 50 °C to 250 °C at the rate of 20 °C/min under a nitrogen atmosphere with flow rate of 30 mL/min. The curve of heat flow shows a broad peak from 60 °C to 180 °C, indicating that the air-dried sample contained a small amount of residual water. The integration of the endothermic transition ranging from 60 °C to 180 °C gives the enthalpy for evaporation of the residual water per unit mass of the dry sample (with residual water) $H_{residual}$. Therefore, the mass of the residual water $m_{residual}$ can be calculated as $m_{residual} = m \cdot H_{residual} / H^0_{water}$, where $H^0_{water} = 2260$ J/g is the latent heat of water evaporation. The curve of heat flow shows another narrow peak ranging from 200 °C to 250 °C, corresponding to the melting of the crystalline domains. The integration of the endothermic transition ranging from 200 °C to 250 °C gives the enthalpy for melting the crystalline domains per unit mass of the dry sample (with residual water) $H_{crystalline}$. Therefore, the mass of the crystalline domains $m_{crystalline}$ can be calculated as $m_{crystalline} = m \cdot H_{crystalline} / H^0_{crystalline}$, where $H^0_{crystalline} = 138.6$ J/g is the enthalpy of fusion of 100 wt.% crystalline PVA measured at the equilibrium melting point T^0_m (5). Therefore, the crystallinity in the ideally dry sample X_{dry} (without residual water) can be calculated as $X_{dry} = m_{crystalline} / \left(m - m_{residual}\right)$. With measured water content from TGA, the crystallinity in the swollen state can be calculated as $X_{swollen} = X_{dry} \cdot \left(1 - \phi_{water}\right)$.

3D printing meshes of PVA hydrogels. The microstructures of PVA hydrogels were fabricated by printing a 3D structure onto a glass slide (Corning). Print paths were generated via production of G-code that controls the XYZ motion of the 3D robotic gantry (Aerotech). G-code was either generated by manual coding or open-source software (Slic3r). The prepared PVA inks were stored in 5 mL syringe barrels, which fitted the nozzles with diameters of 400 μm (EFD Nordson). To achieve stable and optimal printing, we chose 50 kPa of air pressure (Ultimus V, Nordson EFD) as the printing pressure, and 15 wt% PVA (146 kDa, 99% hydrolysis ratio) aqueous solution as the printing ink. After deposition, the printed samples underwent five cycles of freezing (-20 °C for 8 hours) and thawing (20 °C for 3 hours) to achieve the final PVA hydrogel meshes. The prestretched PVA meshes were acquired by applying cyclic prestretching of 3.5 over 1000 cycles on the dogbone-shaped pristine mesh in both in-plane directions.

	Strain-stiffening hydrogels[6,7]	**Bottlebrush elastomers**[8,9]	**Tough hydrogels**[10,11]	**Hydrogel composites**[12,13]	**Nanocrystalline hydrogels**[3]	**Muscle-like hydrogels**
E (kPa) Young's modulus	0.01-0.5	1-100	10-100	1000-10,000	1000-10,000	200
W (wt %) Water content	> 99	0	90	60-80	60-70	84
S (kPa) Nominal strength	~ 0.2	10-100	100-1000	1000-10,000	4000-10,000	5200
Γ_0 (J/m^2) Fatigue threshold	~ 1	~ 10	50-400	~ 1000	400-1000	1250

Table S1. Comparison of combinational properties in various soft materials. Comparison of Young's moduli, water contents, nominal strengths, and fatigue thresholds of strain-stiffening hydrogels (6, 7), bottlebrush elastomers (8, 9), tough hydrogels (10, 11), hydrogel composites (12, 13), nanocrystalline hydrogels (4), and muscle-like hydrogels in this work.

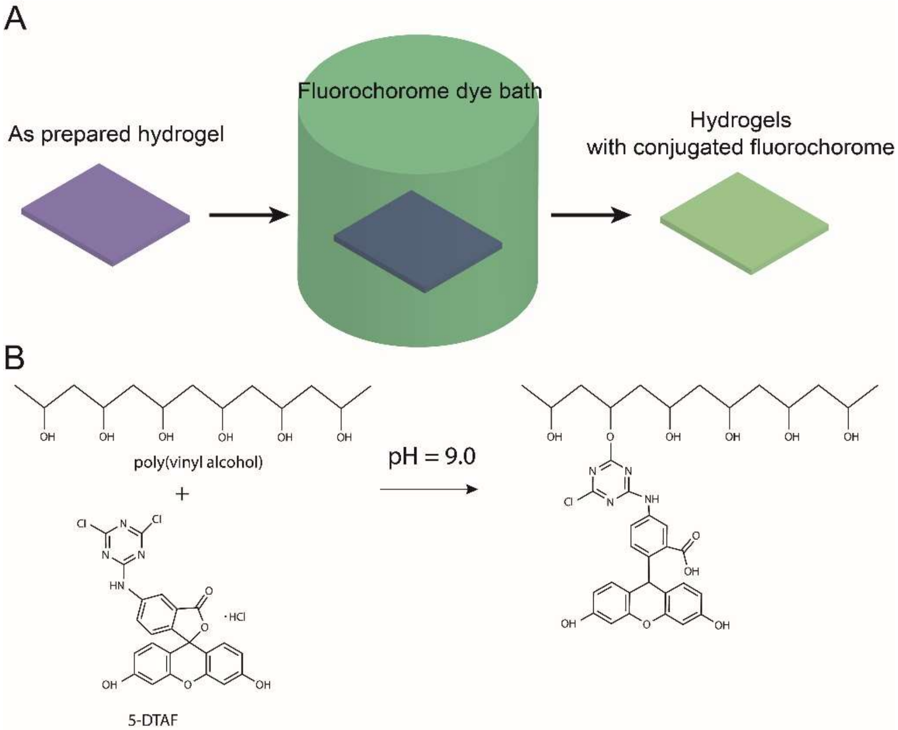

Fig. S1. Conjugation of fluorochoromes on PVA for confocal imaging. *(A)* The fabrication method to introduce conjugated fluorochoromes on PVA polymer chains. *(B)* The chemical reaction for conjugation of fluorochorome on PVA.

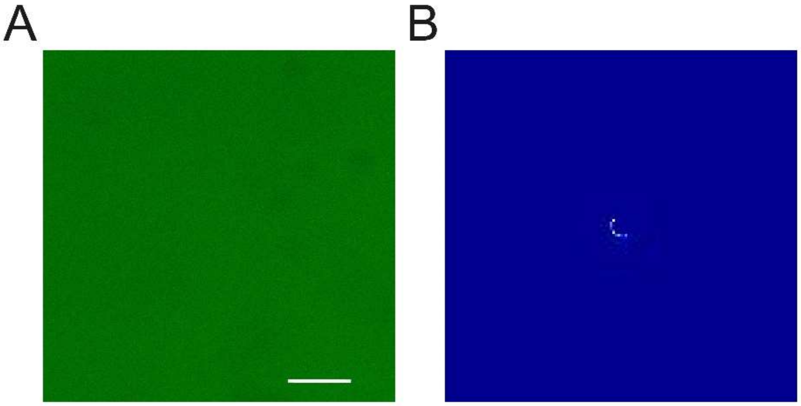

Fig. S2. Morphology characterization of chemically cross-linked PVA hydrogel. *(A)* Confocal image. *(B)* SAXS pattern.

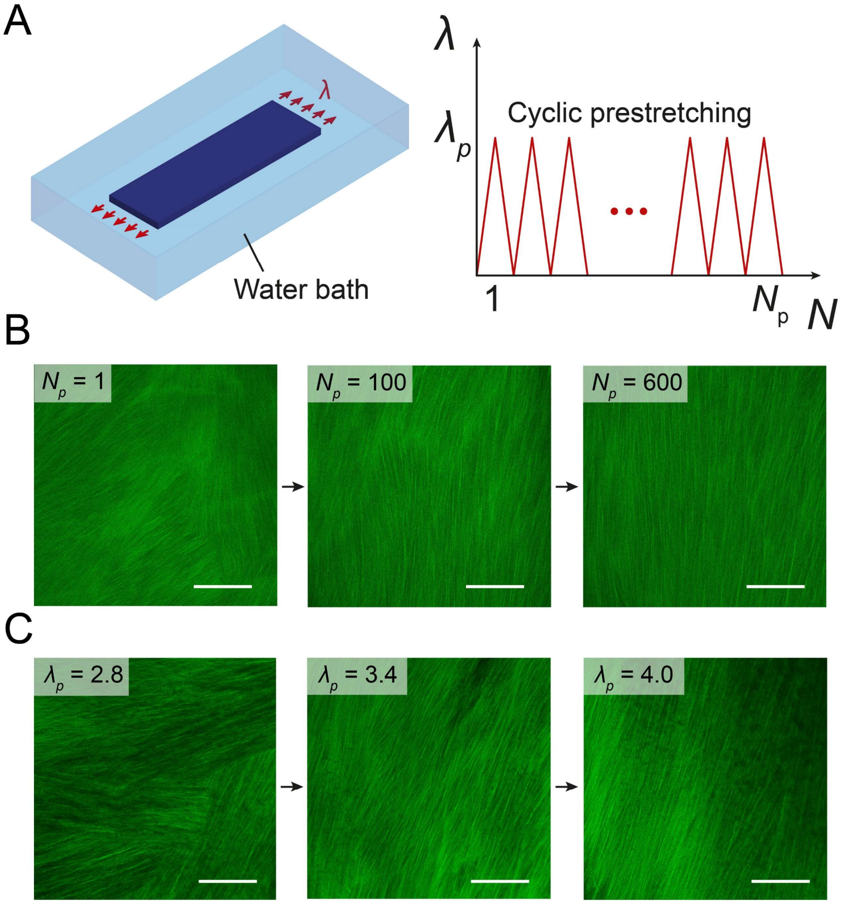

Fig. S3. The effect of applied prestretch and cycle number on the alignment of nanofibrils in PVA hydrogels. *(A)* Schematic illustration of mechanical training of hydrogels to form aligned nanofibrils. *(B)* Confocal images of the PVA hydrogels after 1, 100 and 600 cycles of prestretches of 4.6. *(C)* Confocal images of the PVA hydrogels after 1000 cycles of prestretches of 2.8, 3.4 and 4.0.

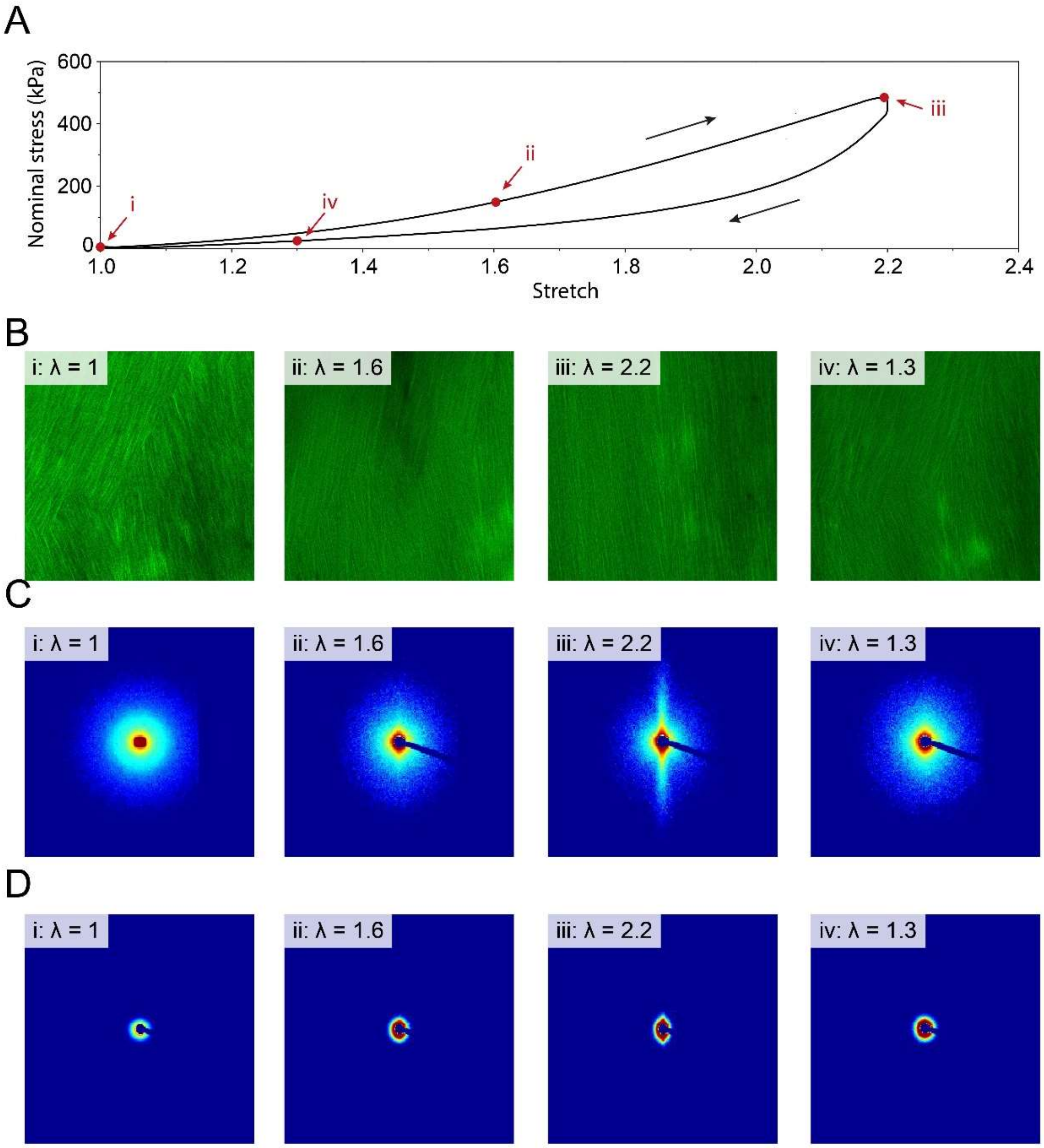

Fig. S4. Confocal images, SAXS, and WAXS patterns of the freeze-thawed PVA hydrogel under a single cycle of load. *(A)* Representative stress vs. stretch curve of the freeze-thawed PVA hydrogel. *(B)* Confocal images, *(C)* SAXS patterns, and *(D)* WAXS patterns of the freeze-thawed PVA hydrogel at the applied stretch of i: λ = 1, ii: λ = 1.6, iii: λ = 2.2 under loading and at the applied stretch of iv: λ = 1.3 under unloading.

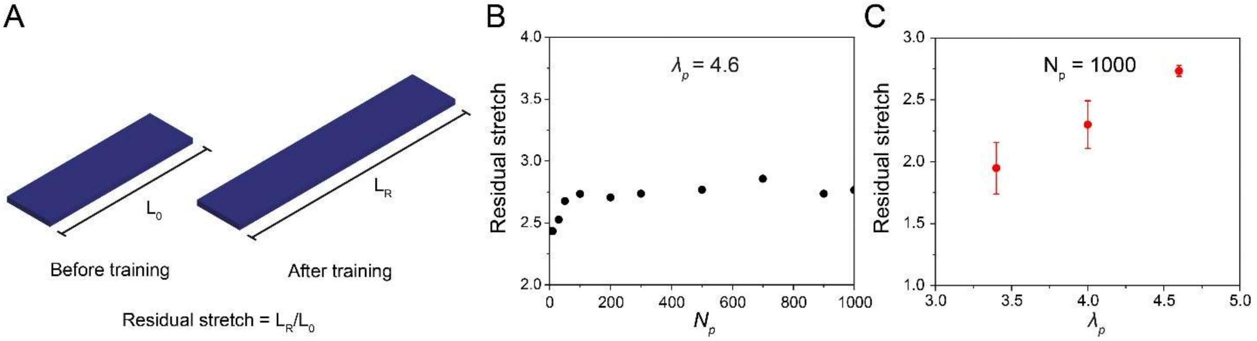

Fig. S5. Residual stretch of prestretched PVA hydrogels. *(A)* The residual stretch is defined as the ratio of the length at undeformed state after training L_R over the length at undeformed state before training L_0. *(B)* Residual stretch after N_p cycles of applied prestretches of 4.6. *(C)* Residual plastic stretch after 1000 cycles of prestretches of λ_p .

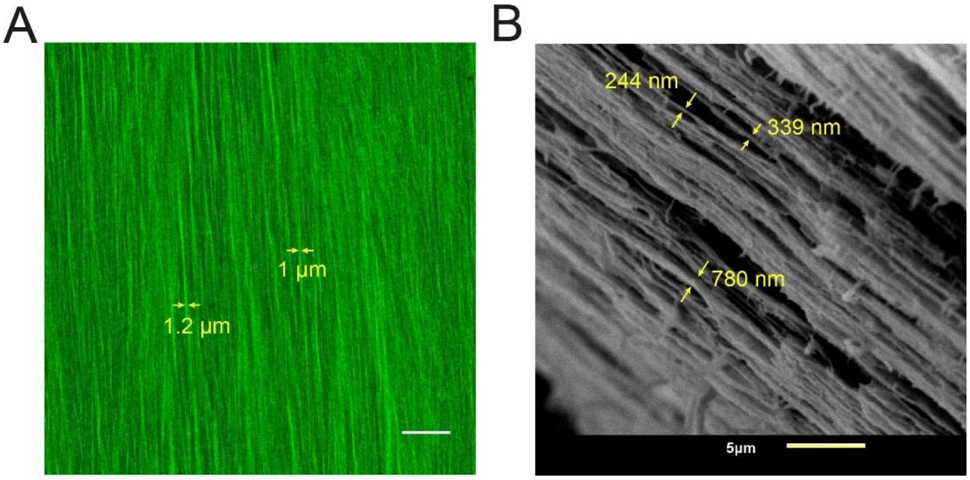

Fig. S6. Measurement of nanofibril diameters in the prestretched PVA hydrogel. *(A)* Confocal image. *(B)* SEM image. The sample for SEM imaging was first mechanically stretched to induce delamination of nanofibrils, and immediately crosslinked by glutaraldehyde to avoid further collapse during supercritical drying, followed by SEM observation. The measured diameters of aligned nanofibrils in the hydrogel range from ~100 nm to ~1 µm. Scale bar is 20 µm in *(A)* and 5 µm in *(B)*.

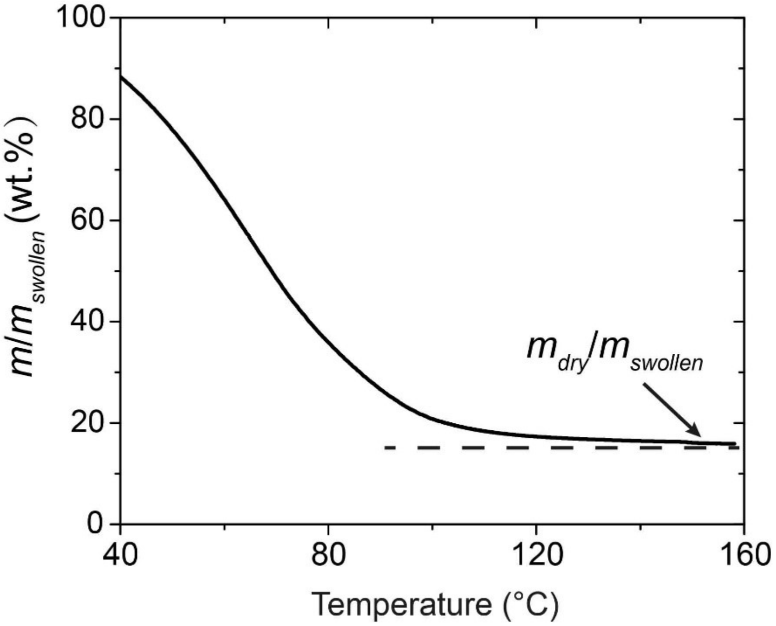

Fig. S7. Representative thermal gravimetric analysis (TGA) curve of the freeze-thawed PVA hydrogel. m, m_{swollen}, and m_{dry} denote the mass of the sample during TGA measurement, in the swollen state, and in fully dry state, respectively.

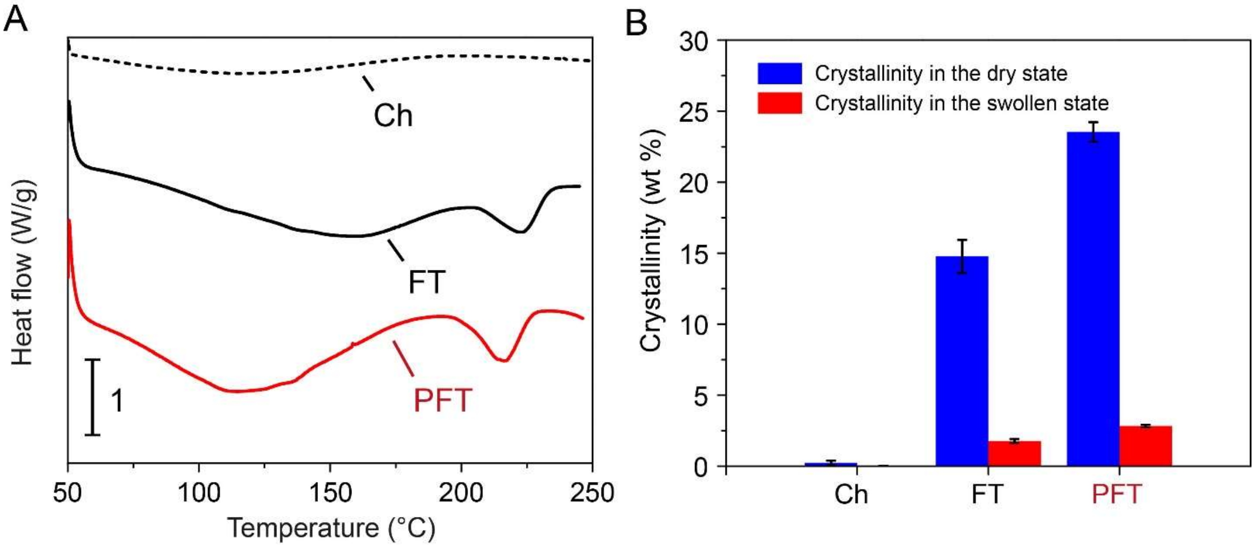

Fig. S8. Measurement of crystallinities in PVA hydrogels. *(A)* Differential scanning calorimetry (DSC) thermographs of chemically cross-linked (i.e., Ch), freeze-thawed (i.e., FT), and prestretched PVA hydrogels (i.e., PFT). *(B)* Summarized crystallinities in the dry state and crystallinities in the swollen state of Ch, FT, and PFT hydrogels.

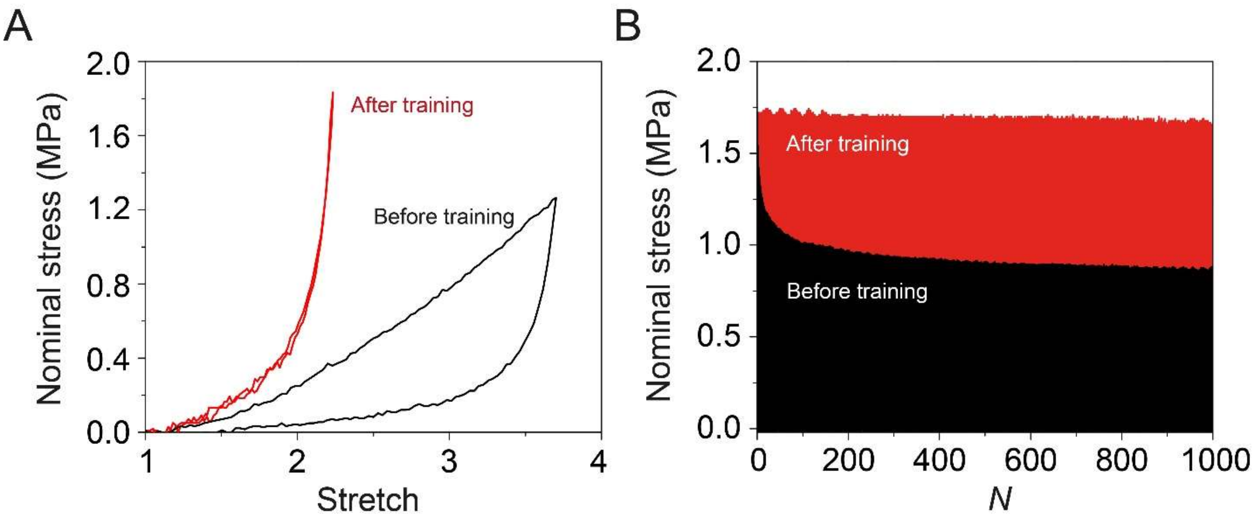

Fig. S9. Comparison of hysteresis in PVA hydrogels before and after mechanical training. *(A)* Loading-unloading nominal stress versus stretch curves of PVA hydrogels before and after training. *(B)* Nominal stress over loading cycles of PVA hydrogels before and after training with maximum applied stretch of 4.5 and 2.2, respectively.

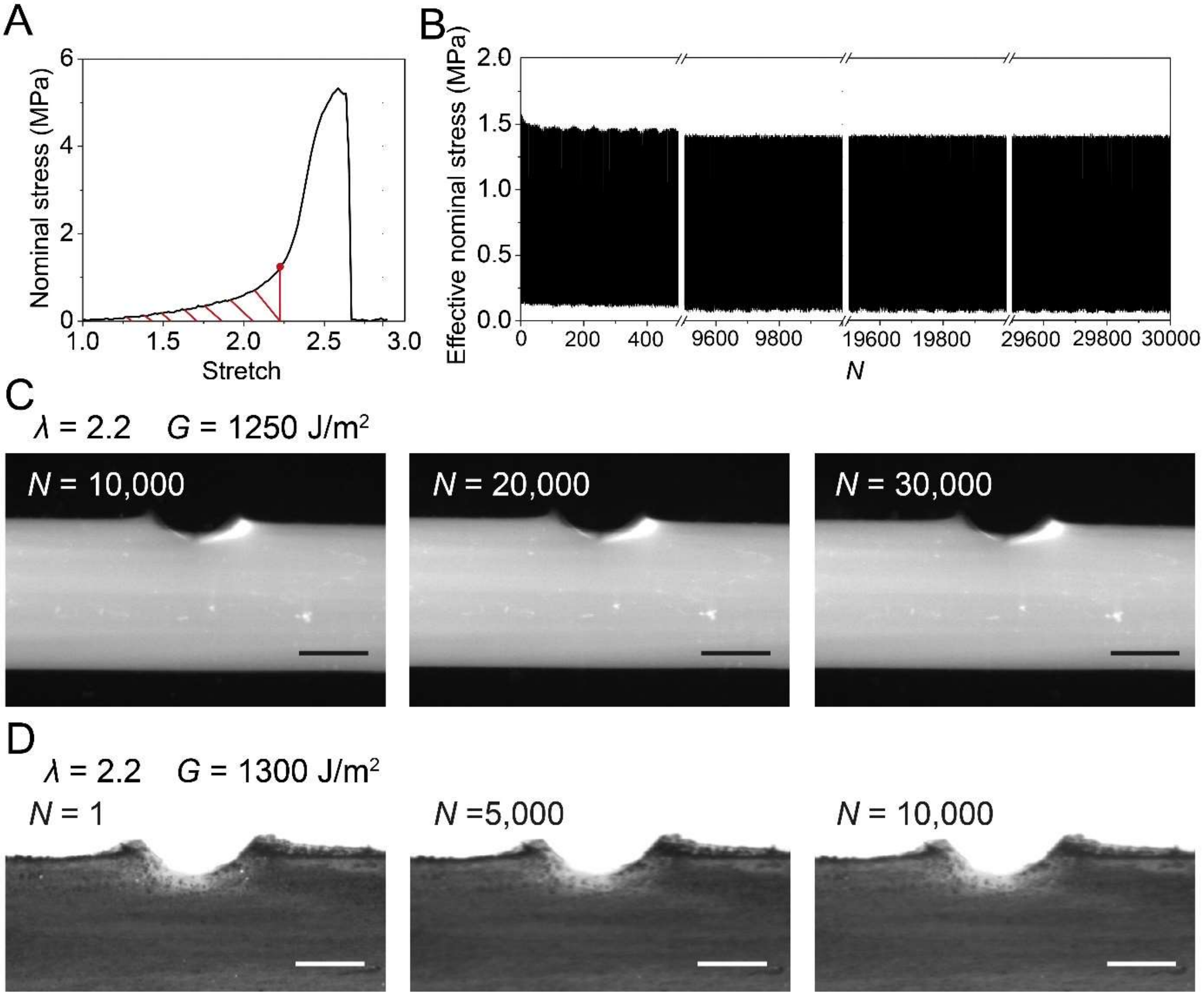

Fig. S10. Validation of high fatigue threshold of the prestretched PVA hydrogel. *(A)* Nominal stress versus stretch of the prestretched PVA hydrogel after prolonged cycles of 1000. The enclosed area indicated by red line denotes the strain energy at the applied stretch of 2.2, i.e., $W\left(\lambda = 2.2\right) = \int_{1}^{2.2} S d\lambda$. *(B)* The effective nominal stress $F/((W\text{-}c)t)$ versus cycle number N of the prestretched PVA hydrogel with a pre-crack c of 0.7 mm, where F is the measured force, W is the sample width, and t is the sample thickness. *(C)* Images of prestretched PVA hydrogel with a pre-crack at the applied energy release rate of 1250 J/m^2 at the cycle number of 10,000, 20,000, and 30,000. (D) Images of another prestretched PVA hydrogel with a pre-crack at the applied energy release rate of 1300 J/m^2 at the cycle number of 1, 5,000, and 10,000. High-contrast graphite speckle patterns were applied to surfaces of samples, validating no observable crack propagation. Scale bars in *(C)* and (*D*) are 1 mm.

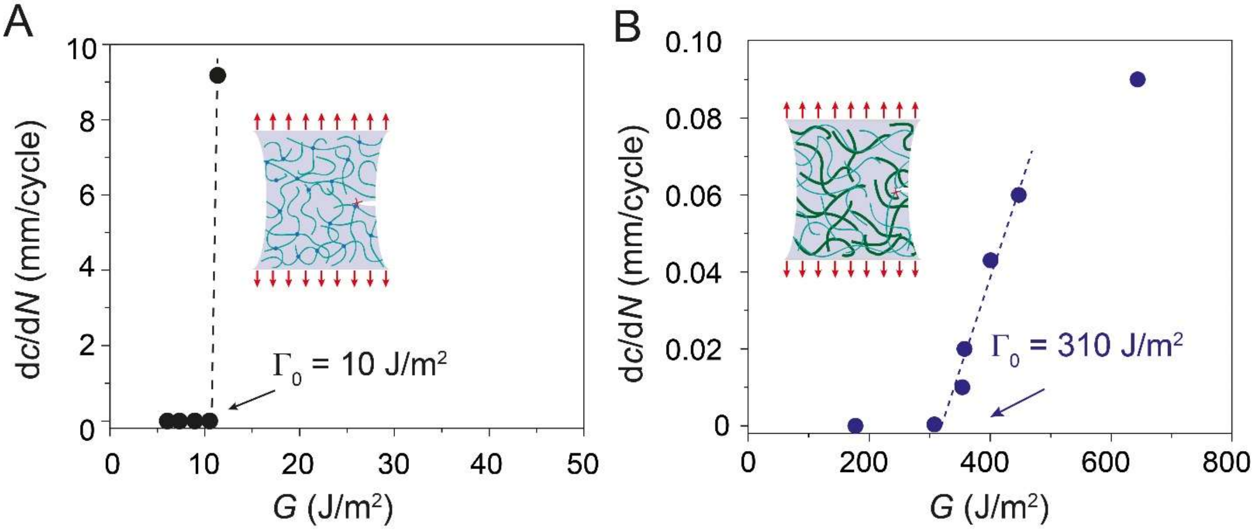

Fig. S11. Fatigue thresholds of PVA hydrogels. *(A)* Chemically cross-linked PVA hydrogel. *(B)* Freeze-thawed PVA hydrogel.

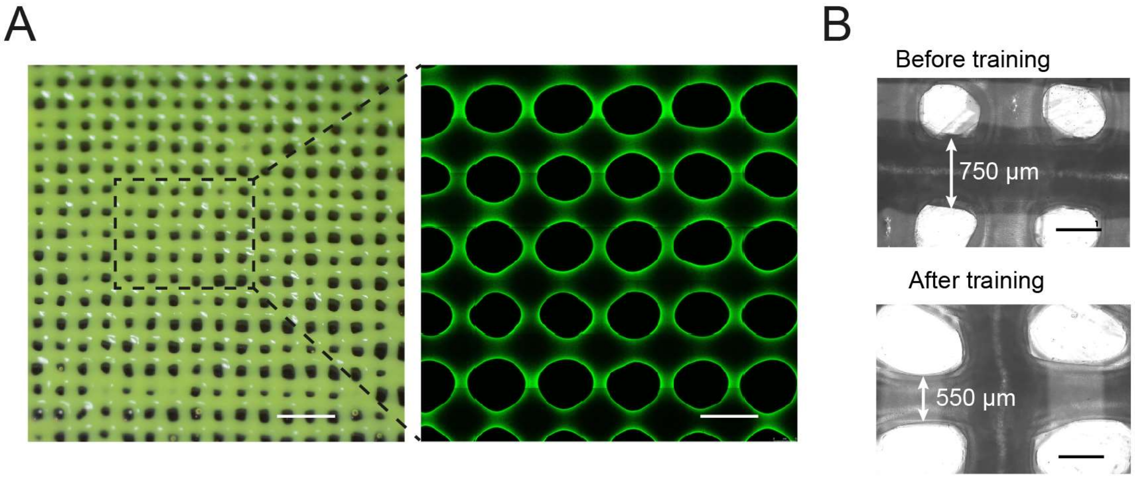

Fig. S12. 3D printing of PVA hydrogels into microstructures. *(A)* Optical image (left) and confocal image (right) of 3D printed PVA meshes (filling ratio: 50%). *(B)* Comparison of optical images of 3D printed mesh before and after mechanical training. Scale bars are 3 mm for left image and 500 µm for right image in *(A)*, 500 µm in *(B)*.

Legends for Supplementary Movie

Movie S1. Cyclic loading of the trained PVA mesh.

References

1. Yang W*, et al.* (2015) On the tear resistance of skin. *Nat Commun* 6:6649.
2. Lake G & Lindley P (1965) The mechanical fatigue limit for rubber. *J Appl Polym Sci* 9:1233-1251.
3. Wang Z*, et al.* (2019) Stretchable materials of high toughness and low hysteresis. *Proc Natl Acad Sci USA* 201821420.
4. Lin S*, et al.* (2019) Anti-fatigue-fracture hydrogels. *Sci Adv* 5:eaau8528.
5. Peppas NA & Merrill EW (1976) Differential scanning calorimetry of crystallized PVA hydrogels. *J. Appl. Polym. Sci.* 20:1457-1465.
6. Jaspers M*, et al.* (2014) Ultra-responsive soft matter from strain-stiffening hydrogels. *Nat Commun* 5:5808.
7. Kouwer PH*, et al.* (2013) Responsive biomimetic networks from polyisocyanopeptide hydrogels. *Nature* 493:651.
8. Vatankhah-Varnosfaderani M*, et al.* (2017) Mimicking biological stress–strain behaviour with synthetic elastomers. *Nature* 549:497.
9. Vatankhah-Varnosfaderani M*, et al.* (2018) Chameleon-like elastomers with molecularly encoded strain-adaptive stiffening and coloration. *Science* 359:1509-1513.
10. Sun J-Y*, et al.* (2012) Highly stretchable and tough hydrogels. *Nature* 489:133.
11. Gong JP, Katsuyama Y, Kurokawa T, & Osada Y (2003) Double-network hydrogels with extremely high mechanical strength. *Adv Mater* 15:1155-1158.
12. Huang Y*, et al.* (2017) Energy-dissipative matrices enable synergistic toughening in fiber reinforced soft composites. *Adv Funct Mater* 27:1605350.
13. Lin S*, et al.* (2014) Design of stiff, tough and stretchy hydrogel composites via nanoscale hybrid crosslinking and macroscale fiber reinforcement. *Soft Matter* 10:7519-7527.